

# On the dust of tailless Oort-cloud comet C/2020 T2 (Palomar)

Yuna G. Kwon<sup>1\*</sup>, Joseph R. Masiero<sup>2</sup>, and Johannes Markkanen<sup>1,3</sup>

<sup>1</sup> Institut für Geophysik und Extraterrestrische Physik, Technische Universität Braunschweig, Mendelssohnstr. 3, 38106 Braunschweig, Germany

e-mail: y.kwon@tu-braunschweig.de

<sup>2</sup> Caltech/IPAC, 1200 E California Blvd, MC 100-22, Pasadena, CA 91125, USA

<sup>3</sup> Max Planck Institute for Solar System Research, Justus-von-Liebig-Weg 3, 37077 Göttingen, Germany

Received August 31, 2022 / Accepted October 25, 2022

## ABSTRACT

We report our new analysis of Oort-cloud comet C/2020 T2 (Palomar) (T2) observed at 2.06 au from the Sun (phase angle of  $28.5^\circ$ ) about two weeks before perihelion. T2 lacks a significant dust tail in scattered light, showing a strong central condensation of the coma throughout the apparition, reminiscent of so-called Manx comets. Its spectral slope of polarized light increases and decreases in the  $J$  ( $1.25 \mu\text{m}$ ) and  $H$  ( $1.65 \mu\text{m}$ ) bands, respectively, resulting in an overall negative (blue) slope ( $-0.31 \pm 0.14 \% \mu\text{m}^{-1}$ ) in contrast to the red polarimetric color of active comets observed at similar geometries. The average polarization degree of T2 is  $2.86 \pm 0.17 \%$  for the  $J$  and  $2.75 \pm 0.16 \%$  for the  $H$  bands. Given that near-infrared wavelengths are sensitive to the intermediate-scale structure of cometary dust (i.e., dust aggregates), our light-scattering modeling of ballistic aggregates with different porosities and compositions shows that polarimetric properties of T2 are compatible with low-porosity ( $\sim 66\%$ ), absorbing dust aggregates with negligible ice contents on a scale of  $10\text{--}100 \mu\text{m}$  (density of  $\sim 652 \text{ kg m}^{-3}$ ). This is supported by the coma morphology of T2 which has a viable  $\beta$  (the relative importance of solar radiation pressure on dust particles) range of  $\lesssim 10^{-4}$ . Secular evolution of  $r$ -band activity of T2 from archival data reveals that the increase in its brightness accelerates around 2.4 au pre-perihelion, with its overall dust production rate  $\geq 100$  times smaller than those of active Oort-cloud comets. We also found an apparent concentration of T2 and Manx comets toward ecliptic orbits. This paper underlines the heterogeneous nature of Oort-cloud comets which can be investigated in the near future with dedicated studies of their dust characteristics.

**Key words.** comets: general – comets: individual: C/2020 T2 (Palomar) – methods: observational, numerical – techniques: polarimetric, spectroscopic

## 1. Introduction

Comets preserve the least-altered planetesimals from the nascent solar system. In particular, comets from the Oort cloud (Oort-cloud comets, OCCs), a reservoir of objects at the outskirts of the solar system ( $\sim 10^3\text{--}5$  au from the Sun; Dones et al. 2015), spent most of their lives in places where sunlight hardly reaches, making them one of the most important classes of primitive objects to connect their properties back to the early solar system environment. This motivates the upcoming ‘Comet Interceptor’ mission, nominally scheduled for launch in 2029, to explore the early solar system environment via OCCs (Snodgrass & Jones 2019).

Observations over the past decades have revealed a heterogeneous nature in OCCs. Departing from the traditional view of comets extending a conspicuous dust tail thousands of kilometers from the nuclei (Krishna Swamy 2010), OCCs in a low-to-moderate activity level (e.g. Licandro et al. 2019; Garcia et al. 2020) or even without dust tails (so-called Manx comets; Meech et al. 2016) have been found, implying a variety of origins for comets found in the present-day Oort cloud. Given the lack of in-situ data on OCCs, characterization of their dust constituents and context are of particular importance for a better understanding of their formation and subsequent evolutionary history and support of future space missions.

Here we report a new near-infrared spectropolarimetric observation of Oort-cloud comet C/2020 T2 (Palomar) (hereafter T2) obtained about two weeks before perihelion ( $q = 2.05$  au). Spectropolarimetry provides a degree of linear polarization as a function of wavelength, which is independent of the number density of dust particles but sensitively depends on their microphysical properties (size, structure, and composition; Kiselev et al. 2015; Kwon et al. 2022). Together with archival data and modeling of both the light scattered by dust and the dust motion in the coma, we aim to constrain the dust environment of T2 and compare its properties with other OCC observations.

## 2. Observations and Data Analysis

A one-epoch low-resolution ( $\lambda/\Delta\lambda \sim 100$ ) near-infrared ( $\sim 1.1\text{--}1.9 \mu\text{m}$ ) spectropolarimetric observation of T2 was conducted on UT 2021 June 26.2 using a spectropolarimeter attached to the 5.1-m diameter Hale Telescope at Palomar Observatory ( $116^\circ 51' 54''\text{W}$ ,  $33^\circ 21' 23''\text{N}$ , 1 712 m). WIRC+Pol is a newly commissioned spectropolarimetry mode of the Wide-field InfraRed Camera (WIRC; Wilson et al. 2003) with a field of view of  $4/3 \times 4/3$  and seeing-limited angular resolution of  $\approx 1''.2$ , located at the prime focus of the telescope (Tinyanont et al. 2019). It measures full linear Stokes parameters ( $I$ ,  $Q$ , and  $U$ ) as a function of wavelength with one exposure, making resulting datasets free from sky rotation during a sequential exposure of images. A half-wave plate (HWP) rotates the incoming light by four differ-

\* Alexander von Humboldt Postdoctoral Fellow

**Table 1.** Geometry and instrument settings of the observations of C/2020 T2 (Palomar)

Telescope/ Instrument	Mode	Filter	Median UT	$N$	Exptime (sec)	$X$	$m_V$ (mag)	$r_H$ (au)	$\Delta$ (au)	$\alpha$ ( $^\circ$ )
Hale/ WIRC+Pol	Spol	$J$	04:58:34	32	960	1.18 (1.13–1.22)	13.623	2.062	1.559	28.5
		$H$	04:58:55	32	960	1.17 (1.15–1.19)				
	Img	$J$	05:25:08	4	120	1.24 (1.23–1.24)				

**Notes.** Top headers: Modes, ‘Spol’ and ‘Img’ denote spectropolarimetric and imaging observations, respectively;  $N$ , number of exposures; Exptime, the total on-source time in seconds ( $=N \times 30$  sec);  $X$ , average airmass with its range in the bracket;  $m_V$ , apparent total  $V$ -band magnitude provided by the JPL Horizons (<http://ssd.jpl.nasa.gov/?horizons>);  $r_H$  and  $\Delta$ , heliocentric and geocentric distances in au, respectively;  $\alpha$ , phase angle (angle of Sun–comet–observer) in degrees.

ent angles ( $2\theta_{\text{HWP}}$ , where  $\theta_{\text{HWP}} = 0^\circ, 22:5, 45^\circ, 67:5$ ) that allows for beam-swapping and improved calibration. Each of the four beams then passes a quarter-wave plate, so-called PG (acting as a beam-splitting polarizer and a grating simultaneously), and an opaque mask in a row, thereby leaving their trace in four quadrants on the CCD, 3’ away from one another (Fig. 1 in Tinyanont et al. 2019). We obtained 32 dithered images (16 each in slit A and B positions) in the  $J$  and  $H$  bands to subtract background signals. More details of the observing strategy can be found in Masiero et al. (2022). The observation journal is summarized in Table 1.

Basic calibration, spectral extraction, and polarimetric calculation were all performed in the WIRC+Pol Data Reduction Pipeline<sup>1</sup>, whose details are described in Tinyanont et al. (2019). An additional correction was made to residual offsets in polarization angle by adding 6:101 and 3:416 to the  $J$ - and  $H$ -band values, respectively, based on Figure 3 of Masiero et al. (2022). In the pipeline, Stokes parameters were corrected from the instrumental polarization and polarization efficiency. We extracted spectra of each resolution element in three aperture sizes, corresponding to 850 km, 1 140 km, and 1 420 km in cometocentric distances at the time of our observation, yet the latter of which was discarded due to the significant background emission at  $\geq 1.7 \mu\text{m}$ . To increase the signal-to-noise ratio, we smoothed the extracted spectra over five spectral bins and eliminated the measurements deviating by more than  $5\sigma$ . The resulting polarimetric parameters (the degree of linear polarization and its position angle) were transformed into the scattering plane (a plane containing the Sun–comet–Earth) in the same manner as Chernova et al. (1993).

### 3. Results and Discussion

Figure 1 shows a  $J$ -band composite image of T2. A featureless, spherical coma is notable, distinct from the morphology of typical OCCs (e.g. Bauer et al. 2015). Most of the coma signal comes from the central part within  $\sim 5''$  from the photocenter. Similar trends throughout the apparition of the comet are confirmed from  $r$ -band archival data (Appendix A).

#### 3.1. Polarimetric properties of the coma dust

Figure 2 shows the degree of linear polarization  $P_r$  and its position angle with respect to the normal direction of the scattering plane  $\theta_r$  extracted from two different aperture sizes  $\rho$  as a function of wavelength  $\lambda$ . The  $1\sigma$  intervals of  $\theta_r$  are distributed close

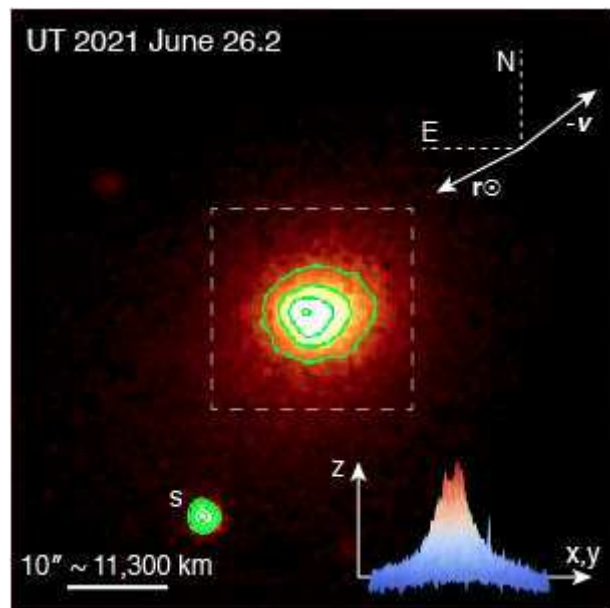


**Fig. 1.**  $J$ -band composite image of T2. The image was boxcar smoothed in the 3-pixel width and overlapped with contours at 90, 50, 25, and 5 % of T2’s peak brightness. ‘S’ marks a background star. A radial profile is given over the inner coma region (enclosed by a dashed-line square of 20’’ by 20’’) in the lower right corner. The negative velocity ( $-v$ ) and solar radius ( $r_\odot$ ) vectors are given.

to zero, which precludes significant dust alignment over the region analyzed and supports the reliability of our data reduction. The two spatial resolutions have almost the same  $P_r$  values at a given wavelength and similar spectral dependence: a slight increase in the  $J$  band (red polarimetric color;  $4.13 \pm 2.11\% \mu\text{m}^{-1}$  for  $\rho = 850$  km and  $8.68 \pm 3.01\% \mu\text{m}^{-1}$  for  $\rho = 1 140$  km) and inflection point around  $1.4 \mu\text{m}$ , followed by a decrease in the  $H$  band (blue polarimetric color;  $-1.59 \pm 1.99\% \mu\text{m}^{-1}$  for  $\rho = 850$  km and  $-1.58 \pm 1.72\% \mu\text{m}^{-1}$  for  $\rho = 1 140$  km). There is a local peak of  $P_r$  ( $\approx 1.5\sigma$  significance) at  $\sim 1.65 \mu\text{m}$  for the inner coma ( $\rho = 850$  km) data. This region corresponds to an absorption peak of crystalline water-ice (Grundy & Schmitt 1998) hosted by a broader  $1.5\text{-}\mu\text{m}$  band that has been observed for several active comets (e.g. Kawakita et al. 2004). We tested different smoothing parameters, but the feature is always present and becomes statistically indistinguishable in the larger aperture size. Although polarimetry is sensitive to the rapid change of the refractive index of scattering materials, in the absence of data covering the region where deeper bands of water ice are expected to

<sup>1</sup> <https://wircpol.readthedocs.io/en/latest/>

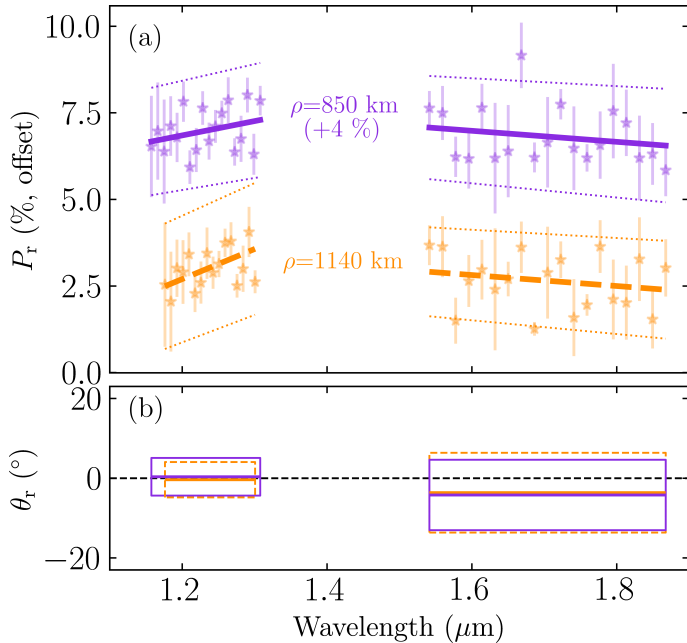


**Fig. 2.** Degree of linear polarization of the dust of T2  $P_r$  and its position angle  $\theta_r$  at a phase angle of  $28.5^\circ$  are given as a function of wavelength  $\lambda$  in Panels a and b, respectively.  $P_r(\lambda)$  extracted from different aperture sizes ( $\rho$ ) are offset for clarity. In Panel a, datapoints in each  $J$ - and  $H$ -band region were fitted by a linear least-square function (given as thick solid and dashed lines), where upper and lower dotted lines indicate  $1\sigma$  intervals. In Panel b, the  $1\sigma$  regions of  $\theta_r$  and their central values are given.

be (1.5 and 2.0  $\mu\text{m}$ ; Mastrapa et al. 2008), we will not consider the weak 1.65  $\mu\text{m}$  peak in the following analysis.

The polarimetric color  $P_r(\lambda)$  of T2 is then compared with those of other OCCs observed at similar geometries (Fig. 3). We selected archival data for which observations at multiple wavelengths were conducted simultaneously (or at least on the same night). For comparison, representative  $P_r$  values of T2 were used by averaging data points in each band:  $2.91 \pm 0.15\%$  for the  $J$  and

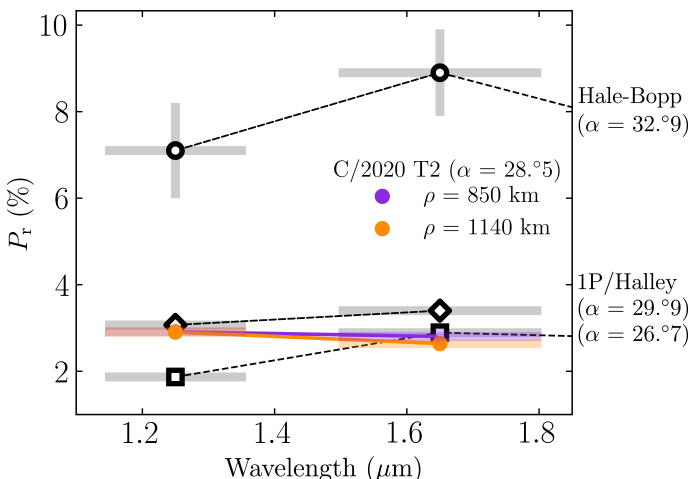


**Fig. 3.** Spectral dependence of the  $P_r$  of T2 and other OCCs: C/1995 O1 (Hale-Bopp) and 1P/Halley. Measurements for other OCCs were obtained from the NASA/PDS comet polarimetric archive (Kiselev et al. 2017): Hale-Bopp from Hasegawa et al. (1997) and 1P/Halley from Brooke et al. (1987) (squares) and Kikuchi et al. (1987) (diamonds), whose phase angles are given in parentheses. The horizontal bars cover the  $J$  and  $H$  bands, while the vertical bars indicate errors in the average value of all data points in each band.

$2.84 \pm 0.14\%$  for the  $H$  bands over  $\rho = 850$  km; and  $2.80 \pm 0.19\%$  for the  $J$  and  $2.62 \pm 0.18\%$  for the  $H$  bands over  $\rho = 1140$  km. Since the two apertures offer consistent values within the errors, we averaged the  $P_r$  at the same band and derived the overall polarimetric color as  $-0.31 \pm 0.14\% \mu\text{m}^{-1}$ . T2's average  $P_r$  values themselves are comparable to those of 1P/Halley, which seems natural for cometary dust in this small  $\alpha$  region, as  $P_r$  begins to show discernible deviations between comets at larger  $\alpha$  ( $\geq 40^\circ$ ; Kiselev et al. 2015), except for the exceptionally high  $P_r$  of Hale-Bopp (Hadamcik et al. 1997). However, the blue  $P_r(\lambda)$  of T2 is in contrast to the dust of OCCs that generally exhibit red polarimetric color over the  $J$  and  $H$  bands.

T2's lower  $H$ -band  $P_r$  as a result of the blue  $P_r(\lambda)$  indicates that its dust has a heterogeneity larger than other cometary dust at the given wavelength (Bohren & Huffman 1983). This can be achieved by its compositional (lower absorptivity, e.g. lower fractions of amorphous carbon or abundant silicates; Rouleau & Martin 1991; Greenberg & Li 1996) and/or mechanical aspects (e.g. higher packing density; Kolokolova & Kimura 2010) to consequently enhance electromagnetic interactions among constituting grains. Compact water ice larger than a few tens of micrometers yields blue  $P_r(\lambda)$  but also increases overall  $P_r$  values (Warren 1984, 2019) and so is not consistent with T2. If the dust is small (of order  $\sim 0.1$ – $1 \mu\text{m}$ ) or fluffy (porosity as low as 2%) it will behave similarly to individual constituting grains in dynamics (Mukai et al. 1992; Skorov et al. 2016) and in light scattering (Kolokolova 2011). It will then provide a red  $P_r(\lambda)$  similar to that of 1P/Halley and Hale-Bopp (Fig. 3). In this case its enhanced thermal emission close to the Sun ( $r_H \lesssim 1$  au) can depolarize signals longward of the  $H$  band (Oishi et al. 1978), but this would not be significant for our T2 observations at 2.06 au from the Sun. Together with the coma morphology (Fig. 1), it is evident for T2 that the observed polarimetric behaviors of its coma cannot be explained by the typical dust properties used to characterize observations of active OCCs.

### 3.2. Quantitative estimations of the optical and dynamical properties of the T2 dust

To reproduce the blue polarimetric color  $P_r(\lambda)$  of T2, we conducted light-scattering modeling of dust aggregates. Presuming that cometary dust is hierarchical (Güttler et al. 2019), a  $>100$ - $\mu\text{m}$  dust agglomerate consists of  $\sim 10$ – $100$ - $\mu\text{m}$  aggregates, each of which is in turn composed of  $\sim 0.1 \mu\text{m}$  grains (monomers). In this regard, near-infrared wavelengths are most sensitive to the intermediate-scale structure (i.e., dust aggregate). We thus considered two types of ballistic aggregates in the same fractal dimension ( $\approx 3$ )<sup>2</sup> and mass but in different porosities (Shen et al. 2008): ballistic aggregate (BA, porosity  $\mathcal{P} \approx 87\%$  and characteristic cluster radius  $R \sim 15.8 \mu\text{m}$ ) and BA with two migrations (BAM2,  $\mathcal{P} \approx 66\%$  and  $R \sim 11.5 \mu\text{m}$ ). The *Rosetta* mission to comet 67P/Churyumov-Gerasimenko showed that monomer size is distributed over  $\sim 0.05$ – $0.6 \mu\text{m}$  but weighted toward smaller size with a mean of  $\sim 0.1 \mu\text{m}$  (Mannel et al. 2019). Due to computational limitations, however, we cannot probe a large aggregate of  $\lesssim 0.1$ - $\mu\text{m}$  monomers. Shen et al. (2008, 2009) verified that the size of monomers would be secondary as long as they

<sup>2</sup> Rosetta observations of coma dust showed particle strength can vary across a large agglomerate, where smaller dust constituents ( $\sim 15$ – $40 \mu\text{m}$ ) have higher strength (Hornung et al. 2016). This makes us exclude fluffy dust (fractal dimension of 1.5–2.5; Güttler et al. 2019), which is relevant to a  $\sim$ millimeter-sized parent dust (Fulle et al. 2015; Mannel et al. 2016), from consideration.

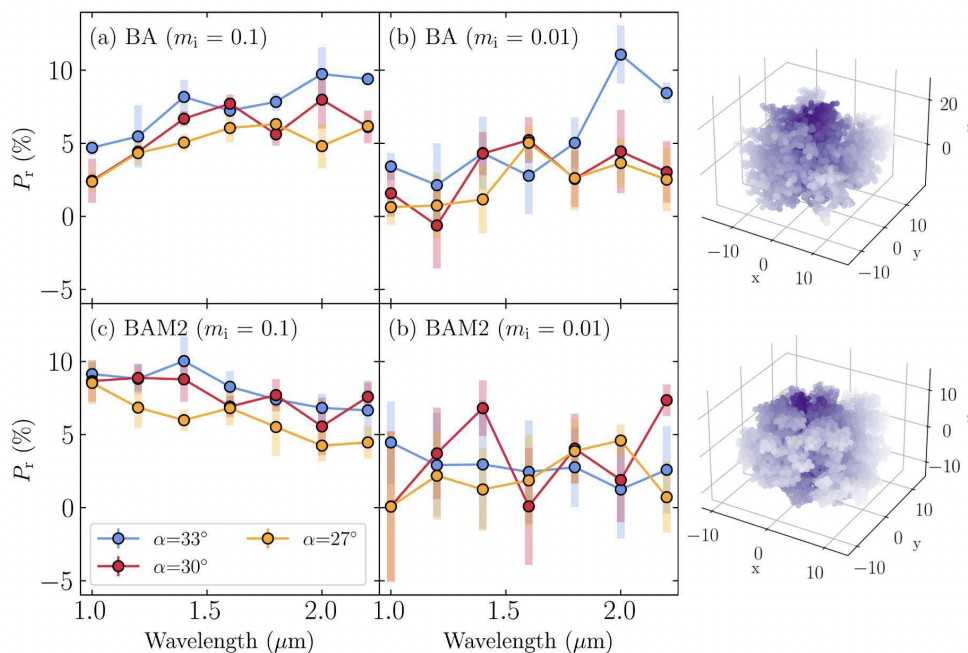


**Fig. 4.** Orientation- and realization-averaged  $P_r$  as a function of wavelength. The upper and lower rows show results for BA and BAM2, respectively, whose geometry is visualized on the rightmost side of the micrometer scale. The left columns display outputs in the standard composition ( $m_r = 1.6$  and  $m_i = 0.1$ ), while the right columns show those with a lower absorptivity ( $m_i = 0.01$ ). Errors indicate  $1\sigma$  for the four realizations of the clusters.

are smaller than the wavelength considered; thus, we considered a simple case of dust clusters consisting of 4 096 spherical monomers of  $0.5\text{-}\mu\text{m}$  in radius<sup>3</sup>. Their geometry (Shen et al. 2008)<sup>4</sup> was randomly generated and averaged over four realizations. For each dust realization, we defined 64 scattering planes (each plane has a constant azimuthal angle  $\phi$ ) and then averaged the outputs. We repeated these processes at 128 random orientations of each dust cluster and averaged the results. We also compared two composition cases: an average complex refractive index of  $m_r = 1.6$  and  $m_i = 0.1$ , which is in the range of the typical cometary dust (e.g. Moreno et al. 2018), and slightly more transparent one ( $m_i = 0.01$ ). The  $4 \times 4$  Mueller matrix was calculated using the fast superposition T-matrix method (FaSTMM; Markkanen & Yuffa 2017).

Figure 4 shows orientation- and realization-averaged  $P_r$  of the modeled dust as a function of wavelength. In the case of the average composition ( $m_i = 0.1$ ), BA has red  $P_r(\lambda)$ , whereas less-porous BAM2 steadily yields blue  $P_r(\lambda)$ . This  $\mathcal{P}-P_r(\lambda)$  relationship is in line with previous studies of dust-rich comets whose high  $P_r$  and red  $P_r(\lambda)$  are associated with the presence of highly porous particles in the coma and for Hale-Bopp with extremely fluffy aggregates (Kiselev et al. 2015 and references therein). In the case of less absorbing dust ( $m_i = 0.01$ ), BA shows slight red  $P_r(\lambda)$  despite large fluctuations due to enhanced interparticle scattering which contributes to an unstable trend<sup>5</sup>, while BAM2 gives either inconsistent or a comparably shallow slope of  $P_r(\lambda)$  to our results. In the absence of other information on T2, this leads us to prefer the standard composition. Slightly higher  $P_r$  values of BAM2 than the observation might not be critical be-

cause in reality scattering dust should be ensembles of aggregates distributed in size, structure, and composition which contain larger heterogeneities than our models and could decrease resulting  $P_r$  (Bohren & Huffman 1983). We do not claim that our BAM2 dust is unique, but it can reproduce the characteristic blue  $P_r(\lambda)$  of T2. Our results thus suggest that the optical properties of the coma dust of T2 are compatible with BAM2-like lower- $\mathcal{P}$  ( $\sim 66\%$ ) dust aggregates, deficient in higher  $\mathcal{P}$  ( $\geq 87\%$ ) ones that are used to describe active comets.

Next, we focus on the coma morphology of T2. At the region of  $\geq 1\ 000$  km from the nucleus, dust trajectories in the coma result from a tug-of-war between outward solar radiation pressure and inward solar gravity forces (Finson & Probst 1968a; Burns et al. 1979). Their mutual effect is parameterized by  $\beta$ , which is the ratio of the former to the latter:

$$\beta \equiv \frac{F_{\text{rad}}}{F_{\text{grav}}} = \frac{3L_{\odot}Q_{\text{pr}}}{16\pi GM_{\odot}c(a\rho_d)} \sim K \cdot (a\rho_d)^{-1}, \quad (1)$$

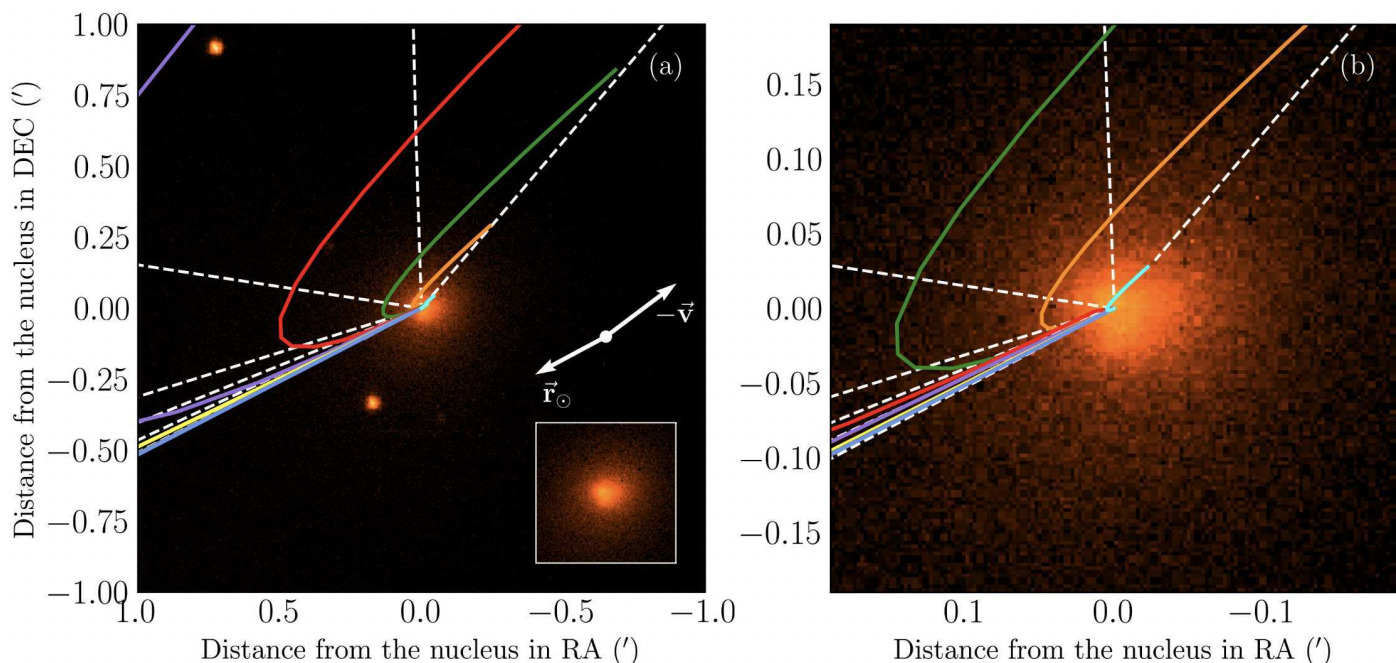
where  $L_{\odot}$  is the solar luminosity,  $Q_{\text{pr}}$  is the dimensionless coefficient of radiation pressure ( $\approx 1$ ),  $G$  is the gravitational constant,  $M_{\odot}$  is the solar mass,  $c$  is the speed of light, and  $a$  and  $\rho_d$  are the radius and density of the dust. Assuming spherical dust with uniform  $\rho_d$ ,  $K$  is  $\sim 5.71 \times 10^{-4} \text{ kg m}^{-2}$  and  $\beta$  becomes a direct function of  $a$  and  $\rho_d$  (which is pertinent to  $\mathcal{P}$ ). With Equation 1, we can specify in each coma region the  $\beta$  of dust having different physical characteristics (syndyne) and ejection times (synchrone). From  $r$ -band archival images showing the onset of discernible activity for T2 began around 3.1 au (Appendix A), we set a simple model with zero ejection velocity where the dust ejection started  $\sim 180$  days prior to our observation. Additional forces that can alter dust motions in the coma (e.g. sublimation and fragmentation) are not considered here.

Figure 5 compares modeled syndynes and synchrone with the T2 image that is the same as Figure 1 but with a twice larger field of view. Only the  $\beta = 10^{-4}$  syndyne reproduces the compact central part of the coma. Its featureless morphology suggests that

<sup>3</sup> We expect  $P_r$  to be independent of the size for larger aggregate scales of interest in typical Halley-dust composition (Mackowski & Kolokolova 2022). This makes us consider a simple dust cluster of monodisperse monomers.

<sup>4</sup> <https://www.astro.princeton.edu/~draine/agglom.html>

<sup>5</sup> In part, resonance effects inside monomers due to the monomer size considered here could contribute to the enhancement of fluctuation.



**Fig. 5.** (a) Synchrone and syndynes of the T2 coma on UT 2021 June 26.2. The dashed lines are synchrone, indicating the locations of dust ejected at different times prior to the observation: 180, 120, 90, 60, 45, 30, 15, and 5 days from right to left. The solid curves are syndynes, where each has a constant  $\beta$  varying from  $10^{-4}$  (low-mobility dust) to 1 (high-mobility dust) anticlockwise from the rightmost. A close-up image is given on the bottom right. (b) Same as T2 in panel a but five times magnified image.

dust particles in the coma were ejected over a wide range of times. The small working  $\beta$  of  $\sim 10^{-4}$  is in accordance with dust that makes up dust trails ( $\sim$ mm-sized dust with  $\beta \lesssim 10^{-4}$ ; Ishiguro et al. 2007) and thus implies that T2 accommodates dust that is less sensitive to solar radiation pressure in its near-nucleus region. This is certainly not typical for the majority of OCCs whose significant dust tails tend to have larger  $\beta$  (Moreno 2022).

In tandem with our light-scattering modeling showing that viable dust in the T2 coma has  $\mathcal{P}$  of  $\sim 66\%$  on the scale of a dust aggregate (order of  $\sim 10$ – $100\ \mu\text{m}$ ; Güttler et al. 2019) in a typical range of the dust composition of comets (Levasseur-Regourd et al. 2018), if we assume that the ice-free dust consists of amorphous carbon (75 vol.%) and Mg-rich silicates (25 vol.%), its approximate density ( $\rho_d = f_C \rho_C + f_{Si} \rho_{Si}$ , where  $f_C$  and  $f_{Si}$  are the volume fractions of amorphous carbon and Mg-rich silicates, respectively, normalized as  $f_C + f_{Si} + \mathcal{P} = 1$ ) is  $\sim 652\ \text{kg m}^{-3}$ . Here we use densities  $\rho_C = 1\ 435\ \text{kg m}^{-3}$  (Jäger et al. 1998) and  $\rho_{Si} = 3\ 360\ \text{kg m}^{-3}$  (Dorschner et al. 1995) and  $\mathcal{P}$  of 66%. Substituting the retrieved density in to  $\rho_d$  in Eq. 1,  $\beta \sim 10^{-4}$  corresponds to the dust size of  $a \sim 270\ \mu\text{m}$ . However, we should be cautious in extrapolating our  $\mathcal{P}$  of dust aggregates to larger dimensions since cometary dust is likely hierarchical structures of heterogeneous dust aggregates rather than a homogeneous conglomerate of sub-micrometer grains (Skorov et al. 2018; Blum et al. 2022).

### 3.3. Possible relationships between the dynamical & dust properties of Oort-cloud comets

Finally, to search for a relationship between the dust properties and orbital distribution of OCCs, information diagnosing their dust characteristics was gleaned from previous observations made in polarimetry and/or mid-infrared spectroscopy. Following the criteria suggested by Kolokolova et al. (2007) and Kwon et al. (2021), we classify comets as ‘Type II’ when they have 1) higher  $P_r$  than the average trend of OCCs at given  $\alpha$ , 2) red  $P_r(\lambda)$ , and/or 3) strong intensity of a  $10\text{-}\mu\text{m}$  silicate emis-

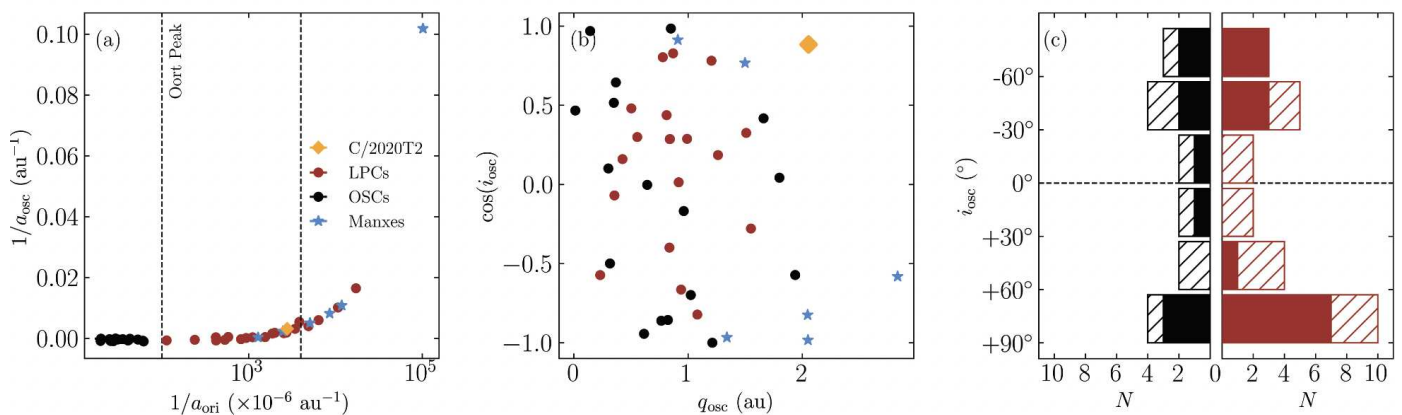
sion feature ( $\geq 1.5$ ; Hanner & Bradley 2004), indicative of high-porosity coma dust; otherwise, they are classified as ‘Type I’ that predominantly eject T2-like lower-porosity dust. Comets with a low-intensity ratio of the  $\text{C}_2$  emission feature to the dust continuum ( $< 500$ ; Krishna Swamy 2010) and a sharp anti-solar dust tail are also grouped as Type II. Six Manx-comet candidates are classified in Type I as their (nearly) tailless morphology akin to T2 indicates that they presumably lack high-porosity dust in the coma (Meech et al. 2016). We only considered comets whose perihelion distance  $q$  is less than 3.1 au for this classification<sup>6</sup>. As a result, a total of 43 OCCs (= 20 Type I + 23 Type II) are selected. Their orbital elements, types, and references are tabulated in Table B.1.

Figure 6a shows a distribution of the reciprocal original semimajor axes  $1/a_{\text{ori}}$  that has a definite correlation with the number of approaches to the Sun (Everhart 1972) and the reciprocal osculating semimajor axes  $1/a_{\text{osc}}$  of the 43 OCCs. The  $1/a_{\text{ori}}$  values are quoted from the Warsaw Catalogue of near-parabolic comets (Królikowska 2014), Minor Planet Center database search engine<sup>7</sup> or Nakano note<sup>8</sup>. The comets are divided into two dynamical groups: Oort-spike comets (OSCs, black circles) inside the classical Oort Peak at  $a_{\text{ori}} \sim 10^4$  au (Oort 1950) and Long-period comets (LPCs, brown circles) outside the peak. The former is often assumed to be dynamically new, though recent studies suggest that the fiducial line of classification should be located farther than the classical one (Dybczyński

<sup>6</sup> As OCCs with  $q > 3.1$  au are located outside the water ice line (Blum et al. 2014; Gundlach et al. 2020), their relatively low activity and lack of dust features shaped by sufficient solar radiation pressure make the classification criteria adopted here hardly applicable. In addition, given that these distant comets are likely to undergo a rapid change of their  $q$  by planet perturbations (Fouchard et al. 2017; Vokrouhlický et al. 2019), we anticipated that their current orbital elements would be less informative.

<sup>7</sup> [https://www.minorplanetcenter.net/db\\_search/](https://www.minorplanetcenter.net/db_search/)

<sup>8</sup> <https://www.oaa.gr.jp/~oaacs/nk.htm>



**Fig. 6.** (a) Distribution of the reciprocal original semimajor axis  $1/a_{\text{ori}}$  and reciprocal osculating semimajor axis  $1/a_{\text{osci}}$  of 43 selected OCCs. The Oort Spike ( $\sim 10^4$  au) and the boundary ( $\sim 250$  au) of planetary regions are marked as the left and right vertical lines, respectively. (b) Distribution of the comets in the plane of the osculating perihelion distance  $q_{\text{osci}}$  and inclination  $\cos(i_{\text{osci}})$ . (c) Distribution of the comets grouped in  $30^\circ$  inclination bins. OSCs and LPCs are shown in the left and right panels, respectively, therein the hatched and filled blocks denote Type I and Type II comets. Detailed classification criteria are explained in the text.

& Królikowska 2015). Another boundary is marked at  $a_{\text{ori}} \sim 250$  au, inside of which the effect of resonances from Neptune outweigh the Oort-cloud processes (e.g. perturbations of passing stars and the Galactic tide; Brassier et al. 2012; Fouchard et al. 2017). The  $a_{\text{ori}}$  of the Manxes and T2 are inside the inner edge of the Oort-cloud at  $\sim 1500$  au (Vokrouhlický et al. 2019).

OSCs and LPCs distribute rather homogeneously in the plane of the current perihelion  $q_{\text{osci}}$  and inclination  $\cos(i_{\text{osci}})$  (Fig. 6b). For Type I (filled black) and Type II (hatched black) comets, there are about 1.5 times as many Type I comets in prograde orbits (Fig. 6c), though the number of comets per bin here would hardly be related to the real architecture of the Oort cloud since we selected comets only for which decent dust analysis has been made. Nonetheless, the relatively high fraction of Type I comets among the considered ones within  $\pm 30^\circ$  from the ecliptic plane, particularly the clustering of all Manx comets and T2 toward the plane, is noteworthy. This apparent clustering in space with their similar  $1/a_{\text{ori}}$  points might reflect their unique origins (Meech et al. 2016) or evolutionary pathways, different from the majority of OCCs ejected from the region of ice-giant planets (Vokrouhlický et al. 2019). More observations are required to exclude possible observational bias (e.g. less active comets might be easier to be detected in low relative velocity space to the Earth?). It will be an interesting topic for future studies to see whether this trend can be retained in larger datasets and thus whether it is more probable to observe less-evolved OCCs near perpendicular to the ecliptic plane.

## 4. Conclusions

This paper reports our tailless Oort-cloud comet C/2020 T2 (Palomar) analysis. The main results are as follows.

1. The  $J$ -band ( $1.25 \mu\text{m}$ ) image of T2 on UT 2021 June 26.2 exhibits tailless morphology, where more than 95 % of light is concentrated in  $\leq 10^4$  km from the nucleus center, reminiscent to the coma morphology of Manx comets (Meech et al. 2016). Secular evolution of its  $r$ -band activity (Appendix A) supports the overall low activity of the comet.
2. Average  $P_r$  of T2 at  $\alpha = 28.5$  is  $2.91 \pm 0.15$  % for the  $J$  and  $2.84 \pm 0.14$  % for the  $H$  bands over  $\rho = 850$  km; and  $2.80 \pm 0.19$  % for the  $J$  and  $2.62 \pm 0.18$  % for the  $H$  bands over  $\rho = 1140$  km. The aperture-averaged polarimetric color over

the  $J$ - $H$  bands is blue ( $-0.31 \pm 0.14 \mu\text{m}^{-1}$ ), opposite to the red polarimetric color of active comets observed at similar  $\alpha$ .

3. From our light-scattering modeling of ballistic aggregates distributed in compositions and porosities and dust dynamic modeling, we suggest that the coma dust of T2 in the near-infrared is compatible with low-porosity ( $\sim 66$  %) dust with typical dust composition ( $\rho_d \sim 625 \text{ kg m}^{-3}$ ). If we assume the uniform distribution in density over the  $10$ – $100 \mu\text{m}$  aggregate scale, the constrained  $\beta \sim 10^{-4}$  corresponds to the viable dust aggregate size of  $\sim 270 \mu\text{m}$ .
4. We found that Manx comets and T2 share dynamical properties to some extent, showing clustering near the ecliptic plane. It appears that a higher percentage of Type I comets occurs within  $30^\circ$  of the plane, which needs to be confirmed with more observations.

*Acknowledgements.* Y. G. K. gratefully acknowledges the support of the Alexander von Humboldt Foundation. J. M. acknowledges funding from the European Union’s Horizon 2020 research and innovation program under grant agreement No 75390 CAStRA. This paper is based in part on observations obtained at the Hale Telescope, Palomar Observatory as part of a continuing collaboration between the California Institute of Technology, NASA/JPL, Yale University, and the National Astronomical Observatories of China.

## References

- A’Hearn, M. F. 1975, *AJ*, 80, 861  
A’Hearn, M. F., Schleicher, D. G., Feldman, P. D., Millis, R. L., & Thompson, D. T. 1984, *AJ*, 89, 579  
Alam, S., Albareti, F. D., Prieto, C. A., et al. 2015, *ApJS*, 219, 12  
Bauer, J. M., Stevenson, R., Kramer, E., et al. 2015, *ApJ*, 814, 85  
Blum, J., Gundlach, B., Mühle, S., & Trigo-Rodríguez, J. M. 2014, *Icarus*, 235, 156  
Blum, J., Bischoff, D., & Gundlach, B. 2022, *Universe*, 8, 381  
Bohren, C., & Huffman, D. 1983, *Absorption and Scattering of Light by Small Particles* (New York: Wiley Sons)  
Borisov, G., Bagnulo, S., Nikolov, P., & Bonev, T. 2015, *P&SS*, 118, 187  
Brassier, R., Duncan, M. J., Levison, H. F., Schwamb, M. E., & Brown, M. E. 2012, *Icarus*, 217, 1  
Brinkman, C. L. 2020, American Astronomical Society Meeting Abstracts #235  
Brooke, T. Y., Knacke, R. F., & Joyce, R. R. 1987, *A&A*, 187, 621  
Bufanda, E., Meech, K., Schambeau, C., et al. 2020, American Astronomical Society Meeting Abstracts #235  
Burns, J. A., Lamy, P. L., & Soter, S. 1979, *Icarus*, 40, 1  
Chernova, G. P., Jockers, K., & Kiselev, N. 1993, *Icarus*, 103, 38  
Deb Roy, P., Halder, P., Das, H. S., & Medhi, B. J. 2015a, *MNRAS*, 450, 1770  
Deb Roy, P., Das, H. S., & Medhi, B. J. 2015b, *Icarus*, 245, 241  
Dones, L., Brassier, R., Kaib, N., & Rickman, H. 2015, *Space Sci. Rev.*, 197, 191

- Dorschner, J., Begemann, B., Henning, T., Jäger, C., & Mutschke, H. 1995, *A&A*, 300, 503
- Dybczyński, P. A., & Królikowska, M. 2015, *MNRAS*, 448, 588
- Everhart, E. 1972, *ApL*, 10, 131
- Finson, M., & Probst, R. 1968a, *ApJ*, 154, 327
- Finson, M., & Probst, R. 1968b, *ApJ*, 154, 353
- Fouchard, M., Rickman, H., Froeschlé, Ch., & Valsecchi, G. B. 2017, *Icarus*, 292, 218
- Fulle, M., Dellar Corte, V., Rotundi, A., et al. 2015, *ApJ*, 802, L12
- Fulle, M., Lazzarin, M., La Forgia, F., et al. 2022, *MNRAS*, 513, 5377
- Furusho, R., Kawakita, H., Fujii, M., et al. 2003, *PASJ*, 55, 1153
- García, R. S., Gil-Hutton, R., & García-Migani, E. 2020, *P&SS*, 180, 104779
- Gehrz, R. D., & Ney, E. P. 1992, *Icarus*, 30, 413
- Geyer, E. H., Jockers, K., Kiselev, N., et al. 1996, *Ap&SS*, 239, 259
- Gibb, E. L., Bonev, B. P., Villanueva, G., et al. 2012, *ApJ*, 750, 102
- Greenberg, J. M., & Li, A. 1996, *A&A*, 309, 258G
- Grundy, W. M., & Schmitt, B. 1998, *J. Geophys. Res.*, 103, 25809
- Gundlach, B., Blum, J., Keller, H. U., & Skorov, Y. et al. 2015, *A&A*, 583, A12
- Gundlach, B., Fulle, M., & Blum, J. 2020, *MNRAS*, 493, 3690
- Güttler, C., Mannel, T., Rotundi, A., et al. 2019, *A&A*, 24, 1
- Hadamcik, E., Lvasseur-Regourd, A.-C., & Renard, J. B. 1997, *EM&P*, 78, 365
- Hadamcik, E., Sen, A. K., Lvasseur-Regourd, A.-C., et al. 2014, *M&PS*, 49, 36
- Hanner, M. S., Newburn, R. L., Gehrz, R. D., et al. 1990, *ApJ*, 348, 312
- Hanner, M. S., Lynch, D. K., & Russell, R. W. 1994, *ApJ*, 425, 274
- Hanner, M. S., & Bradley, J. P. 2004, in *Comets II*, eds. M. Festou, H. U. Keller, & H. A. Weaver (Tucson: University of Arizona Press), 555
- Harker, D. E., Woodward, C. E., Wooden, D. H., et al. 1999, *AJ*, 118, 1423
- Harker, D. E., Wooden, D. H., Woodward, C. E., & Lisse, C. M. 2002, *ApJ*, 615, 1081
- Hasegawa, H., Ichikawa, T., Abe, S., et al. 1997, *E&MP*, 78, 353
- Hornung, K., Merouane, S., Hilchenbach, M., et al. 2016, *PSS*, 133, 63
- Ishiguro, M., Sarugaku, Y., Ueno, M., et al. 2007, *Icarus*, 189, 169
- Ivanova, O., Zubko, E., Videen, G., et al. 2017, *MNRAS*, 469, 2695
- Jäger, C., Mutschke, H., & Henning, T. 1998, *A&A*, 332, 291
- Joshi, U. C., Baliyan, K. S., & Ganesh, S. 2003, *A&A*, 405, 1129
- Kawakita, H., Watanabe, J.-I., Ootsubo, T., et al. 2004, *ApJ*, 60, 191
- Kearns, C. 1958, *PASP*, 70, 202
- Kelley, M. S., Woodward, C. E., Jones, T. J., Reach, W. T., & Johnson, J. 2004, *AJ*, 127, 2398
- Kikuchi, S., Mikami, Y., Mukai, T., Mukai, S., & Hough, J. H. 1987, *A&A*, 187, 689K
- Kiselev, N., & Velichko, F. P. 1997, *EM&P*, 78, 347
- Kiselev, N., & Velichko, F. P. 1998, *Icarus*, 133, 286
- Kiselev, N., Jockers, K., & Rosenbush, V. 2002, *EM&P*, 90, 167
- Kiselev, N., Rosenbush, V., Kolokolova, L., & Lvasseur-Regourd, A.-C. 2015, in *Polarimetry of Stars and Planetary Systems*, eds. L. Kolokolova, J. Hough, & A.-C. Lvasseur-Regourd (Cambridge: Cambridge University Press), 379
- Kiselev, N., Shubina, E., Velichko, S., Jockers, K., Rosenbush, V., and Kikuchi, S. (eds.), *Compilation of Comet Polarimetry from Published and Unpublished Sources*, urn:nasa:pds:compil-comet:polarimetry::1.0, NASA Planetary Data System, 2017
- Kolokolova, L., Kimura, H., Kiselev, N., & Rosenbush, V. 2007, *A&A*, 463, 1189
- Kolokolova, L., & Kimura, H. 2010, *A&A*, 513, A40
- Kolokolova, L. 2011, *ASPC*, 449, 345
- Krishna Swamy, K. S. 2010, *Physics of Comets*, 3rd edn. (Singapore: World Scientific)
- Królikowska, M. 2014, *A&A*, 567, A126
- Królikowska, M. & Dybczyński, P. A. 2017, *MNRAS*, 472, 4634
- Kwon, Y. G., Ishiguro, M., Kuroda, D., et al. 2017, *AJ*, 154, 173
- Kwon, Y. G., Ishiguro, M., Kwon, J., et al. 2019, *A&A*, 629, A121
- Kwon, Y. G., Kolokolova, L., Agarwal, J., & Markkanen, J. 2021, *A&A*, 650, L7
- Kwon, Y. G., Bagnulo, S., Markkanen, J., et al. 2022, *A&A*, 657, A40
- Lamy, P. L., Toth, I., Fernández, Y., & Weaver, H. A. 2004, in *Comets II*, eds. M. Festou, H. U. Keller, & H. A. Weaver (Tucson: University of Arizona Press), 223
- Lvasseur-Regourd, A.-C., Hadamcik, E., & Renard, J. B. 1996, *A&A*, 313, 327
- Lvasseur-Regourd, A. C., Agarwal, J., Cottin, H., et al. 2018, *Space Sci. Rev.*, 214, 64
- Licandro, J., de la Fuente Marcos, C., de la Fuente Marcos, R., et al. 2019, *A&A*, 625, A133
- Lynch, D., Russell, R. W., Hackwell, J. A., Hanner, M. S., & Hammel, H. B. 1992, *Icarus*, 100, 197
- Mackowski, D. W., & Kolokolova, L. 2022, *J. Quant. Spec. Radiat. Transf.*, 287, 108221
- Mannel, T., Bentley, M. S., Schmied, R., et al. 2016, *MNRAS*, 462, 304
- Mannel, T., Bentley, M. S., Boakes, P. D., et al. 2019, *A&A*, 630, 26
- Markkanen, J., & Yuffa, A. J. 2017, *J. Quant. Spec. Radiat. Transf.*, 189, 181
- Martel, M. T. 1960, *Annales d'Astrophysique*, 23, 480
- Masci, F. J., Laher, R. R., Rusholme, B., et al. 2019, *PASP*, 131, 018003
- Masiero, J. R., Tinianont, S., & Millar-Blanchaer, M. A. 2022, *PSJ*, 3, 90
- Mason, C. G., Gehrz, R. D., Ney, E. P., Williams, D. M., & Woodward, C. E. 1998, *ApJ*, 507, 398
- Mason, C. G., Gehrz, R. D., Jones, T. J., et al. 2001, *ApJ*, 549, 635
- Mastrapa, R. M., Bernstein, M. P., Sandford, S. A., et al. *Icarus*, 197, 307
- Mazzotta Epifani, E., Snodgrass, C., Perna, D., et al. 2016, *P&SS*, 132, 23
- Medford, M. S., Lu, J. R., & Schlafly, E. F. 2020, *RNAAS*, 4, 38
- Meech, K. J., Yang, B., Keane, J., et al. 2014, *AAS/Division for Planetary Sciences Meeting Abstracts*, #46, 200.02
- Meech, K. J., Yang, B., Kleya, J., et al. 2016, *Science Advances*, 2, e1600038
- Molnar-Bufanda, E., Meech, K., & Schambeau, C. 2019, *EPSC-DPS Joint Meeting*, id. EPSC-DPS2019-1133
- Moreno, F., Guirado, D., Muñoz, O., et al. *AJ*, 156, 237
- Moreno, F. 2022, *Universe*, 8, 366
- Mukai, T., Ishimoto, H., Kozasa, T., Blum, J., & Greenberg, J. M. 1992, *A&A*, 262, 315
- Ney, E. P. 1974, *Icarus*, 23, 551
- Ney, E. P. 1982, *IAU Colloq. 61: Comet Discoveries, Statistics, and Observational Selection*, 323
- Öhman, Y. 1941, *StoAn*, 13, 11
- Oishi, M., Kawara, K., Kobayashi, Y., et al. 1978, *PASJ*, 30, 149
- Oort, J. H. 1950, *BAN*, 11, 91
- Poch, O., Pommerol, A., Jost, B., et al. 2016a, *Icarus*, 266, 288
- Poch, O., Pommerol, A., Jost, B., et al. 2016b, *Icarus*, 267, 154
- Piro, C., Meech, K. J., Bufanda, E., et al. 2021, *PSJ*, 2, 33
- Rosenbush, V., Rosenbush, A. E., & Dement'ev, M. 1994, *Icarus*, 108, 81
- Rosenbush, V., Kiselev, N., & Velichko, S. 2002, *EM&P*, 90, 423
- Rosenbush, V., Velichko, F. P., Kiselev, N., et al. 2006, *Space Sci. Rev.*, 40, 230
- Rouleau, F., & Martin, P. G. 1991, *ApJ*, 377, 526R
- Roy Choudhury, S., Hadamcik, E., & Sen, A. K. 2015, *P&SS*, 118, 193
- Sekiguchi, T., Miyasaka, S., Dermawan, B., et al. 2018, *Icarus*, 304, 95
- Shen, Y., Draine, B. T., & Johnson, E. T. 2008, *ApJ*, 689, 2605
- Shen, Y., Draine, B. T., & Johnson, E. T. 2009, *ApJ*, 696, 2126S
- Skorov, Y., & Blum, J. 2012, *Icarus*, 221, 1
- Skorov, Y., Reshetnyk, V., Lacerda, P., Hartogh, P., & Blum, J. 2016, *MNRAS*, 461, 3410
- Skorov, Y., Reshetnyk, V., Rezac, L., et al. 2018, *MNRAS*, 477, 4896
- Snios, B., Kharchenko, V., Lisse, C. M., et al. 2016, *ApJ*, 818, 2
- Snodgrass, C., & Jones, G. H. 2019, *Nat. Commu.*, 10, 5418
- Tinyanont, S., Millar-Blanchaer, M. A., Nilsson, R., et al. 2019, *PASP*, 131, 025001
- Tonry, J. L., Stubbs, C. W., Lykke, K. R., et al. 2012, *ApJ*, 750, 99
- Turner, N. J., & Smith, G. H. 1999, *AJ*, 118, 3039
- Velichko, S. F., Kiselev, N., & Velichko, F. P. 2005, *EM&P*, 97, 379
- Velichko, S. F., Kiselev, N., Velichko, F. P., et al. 2012, *Astronomicheskij Tsirkulyar*, 1576
- Vokrouhlický, D., Nesvorný, D., & Dones, L. 2019, *AJ*, 157, 181
- Warren, S. G. 1984, *Appl. Opt.*, 23, 1206
- Warren, S. G. 2019, *Phil. trans. R. Soc. A*, 377, 20180161
- Wilson, J. C., Eikenberry, S. S., Henderson, C. P., et al. 2003, *Proc. SPIE*, 4841, 451
- Wooden, D. H., Woodward, C. E., & Harker, D. E., 2004, *ApJ*, 612, L77
- Wooden, D. H., De Buizer, J., Kelley, M. S., et al. 2014, *Asteroids, Comets, Meteors 2014*
- Woodward, C. E., Kelley, M. S., & Wooden, D. H. 2004, *IAU Circ.* 8378
- Woodward, C. E., Jones, T. J., Brown, B., et al. 2011, *AJ*, 141, 181
- Woodward, C. E., Wooden, E. H., Harker, D. E., et al. 2021, *PSJ*, 2, 25
- Yang, B., Jewitt, D., Zhao, Y., et al. 2021, *ApJ*, 914, L17
- Zhang, Q., Kolokolova, L., Ye, Q., & Vissapragada, S. 2022, *PSJ*, 3, 135

## Appendix A: *r*-band photometry of C/2020 T2 (Palomar)

Secular evolution of cometary activity as a comet approaches the Sun provides insight into how much volatile ices surface retains and thus the degree of processing of the surface layer (Gundlach et al. 2015, 2020). To put our near-infrared spectropolarimetric observation in a broader context, we utilized the *r*-band broadband imaging data of T2 from the Zwicky Transient Facility (ZTF) archive (Masci et al. 2019)<sup>9</sup>. The data cover heliocentric distances  $r_H$  ranging from 3.575 au to 2.075 au between UT 2020 October 23 and UT 2021 August 04, with the comet passing perihelion at  $q = 2.055$  au on UT 2021 July 11.1<sup>10</sup>. ZTF is a 1.2-m diameter time-domain survey telescope, scanning the entire northern visible sky with a pixel scale of  $1''0 \text{ pixel}^{-1}$  and a field of view (FoV) of  $47 \text{ deg}^2$  to a  $5\text{-}\sigma$  median magnitude limit of  $r \sim 21.012 \text{ mags}$ <sup>11</sup>. Since ZTF applies a unified integration time of 30 seconds (Masci et al. 2019), we made use of *r*-band data that generally displays the best signal-to-noise ratio for cometary dust. The archive provides images that are already pre-processed with bias removal, dark subtractions, and flattening. Figure A.1 summarizes the change in the coma morphology of T2 during this period.

T2 became bright enough in the ZTF images to conduct aperture photometry on UT 2020 October 23 at  $r_H \sim 3.6$  au and began to show an extended coma signal around 3.1 au from the Sun. Throughout the apparition, T2 lacked a significant dust tail but showed a modest elongation of the dust coma (Fig. A.1). The oval-shaped coma containing most of the light shows no preference in the elongation direction. In the absence of significant coma features whose signal exceeds the background uncertainty, the coma morphology in the visible light supports the nearly tailless feature of T2 in the near-infrared (Fig. 1).

The evolution of the photometric parameters of T2 is shown in Figure A.2. *r*-band magnitudes of T2 were measured with a fixed aperture size of 10 000 km from the comet center and then corrected by differential magnitudes of background stars by comparing the instrumental magnitude of the comet with the star magnitude provided by the SDSS-12 catalog (Alam et al. 2015). The conversion between magnitudes in different catalogs was made based on the transformation parameters provided by Tonry et al. (2012) and Medford et al. (2020). Reduced *r*-band magnitude as a function of heliocentric distance  $r_H$ ,  $m_r(r_H)$ , was derived by correcting the effect of varying geocentric distance and phase angle over the period as

$$m_r(r_H) = m_r(r_H, \Delta, \alpha) - 5\log_{10}(\Delta) - 2.5\log_{10}(\Phi(\alpha)), \quad (\text{A.1})$$

where  $m_r(r_H, \Delta, \alpha)$  is the apparent magnitude, which is corrected from the differential photometry using the background star catalog and  $\Phi(\alpha)$  is the phase function of the coma dust. We adopted a commonly used empirical scattering phase function ( $2.5 \log_{10}(\Phi(\alpha)) = b\alpha$ ), where the phase coefficient of  $b = 0.035 \text{ mag deg}^{-1}$  was assumed (e.g. Lamy et al. 2004). Given the apparent magnitude, we further derived the so-called  $Af\rho$  parameter ( $A$  is the albedo of dust particles and  $f$  is their packing density within the aperture radius of  $\rho$ ; A'Hearn et al. 1984), a proxy of the dust production rate (Fulle et al. 2022), using Eq. 8 in Kwon et al. (2019), where  $\rho = 10 \text{ 000 km}$  throughout the analysis.

At around 2.4 au, the slope of brightening in the reduced *r*-band magnitude begins to steepen more than two times higher

than at further distances (Fig. A.2). The  $Af\rho$  parameter accordingly exhibits an acceleration around that point, indicative of the discontinuous dust ejection into the coma. The dust production rate, approximated by the  $Af\rho$  parameter, of T2 is  $\geq 100$  times weaker than other OCCs at similar  $r_H$  (Mazzotta Epifani et al. 2016; Garcia et al. 2020; Fulle et al. 2022).

Different types of ice particles sublimate at different temperature environments and thus dominate cometary activity at distinctive distance regimes from the Sun. Supervolatile ice (particularly  $\text{CO}_2$  ice) sublimation is significant until  $\sim 4$  au, followed by the regime where water ice starts to dominate the dust ejection at  $\sim 2.5\text{--}2.7$  au (Blum et al. 2014; Gundlach et al. 2015; Bauer et al. 2015; Gundlach et al. 2020). The observed transitional point of T2 at  $\sim 2.4$  au would signify the onset point of water ice sublimation-driven dust activity of the comet. The very low-activity level outside the transition point implies a dearth of supervolatile ices near the surface dust layer and/or that the upper dust layer through which gas molecules diffuse outward is more consolidated compared to those of other active comets. Both cases indicate that there is a processed surface environment on T2's nucleus. These surface conditions seem to be far different from those of comets that have just completed their gravitational aggregation in the protoplanetary system (Blum et al. 2022 and references therein) or those of comets in early evolutionary phases where their surfaces deplete inherent ice by sublimation but have not yet undergone significant compression that can preserve highly fluffy structures (Skorov & Blum 2012; Poch et al. 2016a,b).

Putting all the results together, T2 appears to share several aspects with so-called Manx comets: not only similar locations in orbital space (Fig. 6) but also their relatively low activity in scattered light than active dust-rich OCCs, (nearly) tailless coma morphology (Meech et al. 2016; Piro et al. 2021), and the existence of a discontinuous, transitional point of the dust ejection in their inbound orbits (e.g. Molnar-Bufanda et al. 2019). All the observations suggest the paucity of highly porous (or ensuing  $\sim 0.1\text{--}1 \mu\text{m}$ -sized small) dust particles in their pre-perihelion comae. Observations of low-activity OCCs in thermal emission (particularly in the mid-infrared of  $5\text{--}20 \mu\text{m}$ ) will provide independent information on how the internal structure and composition of their dust constituents (Gehrz & Ney 1992) differentiate from active OCCs. This will help reveal diversities embedded in the formation and subsequent evolutionary history of comets consisting of the present-day Oort cloud.

## Appendix B: Ancillary information for the comets used in Figure 6

<sup>9</sup> <https://irsa.ipac.caltech.edu/applications/ztf/>

<sup>10</sup> <https://ssd.jpl.nasa.gov/horizons/app.html#/>

<sup>11</sup> <https://www.ztf.caltech.edu/ztf-camera.html>

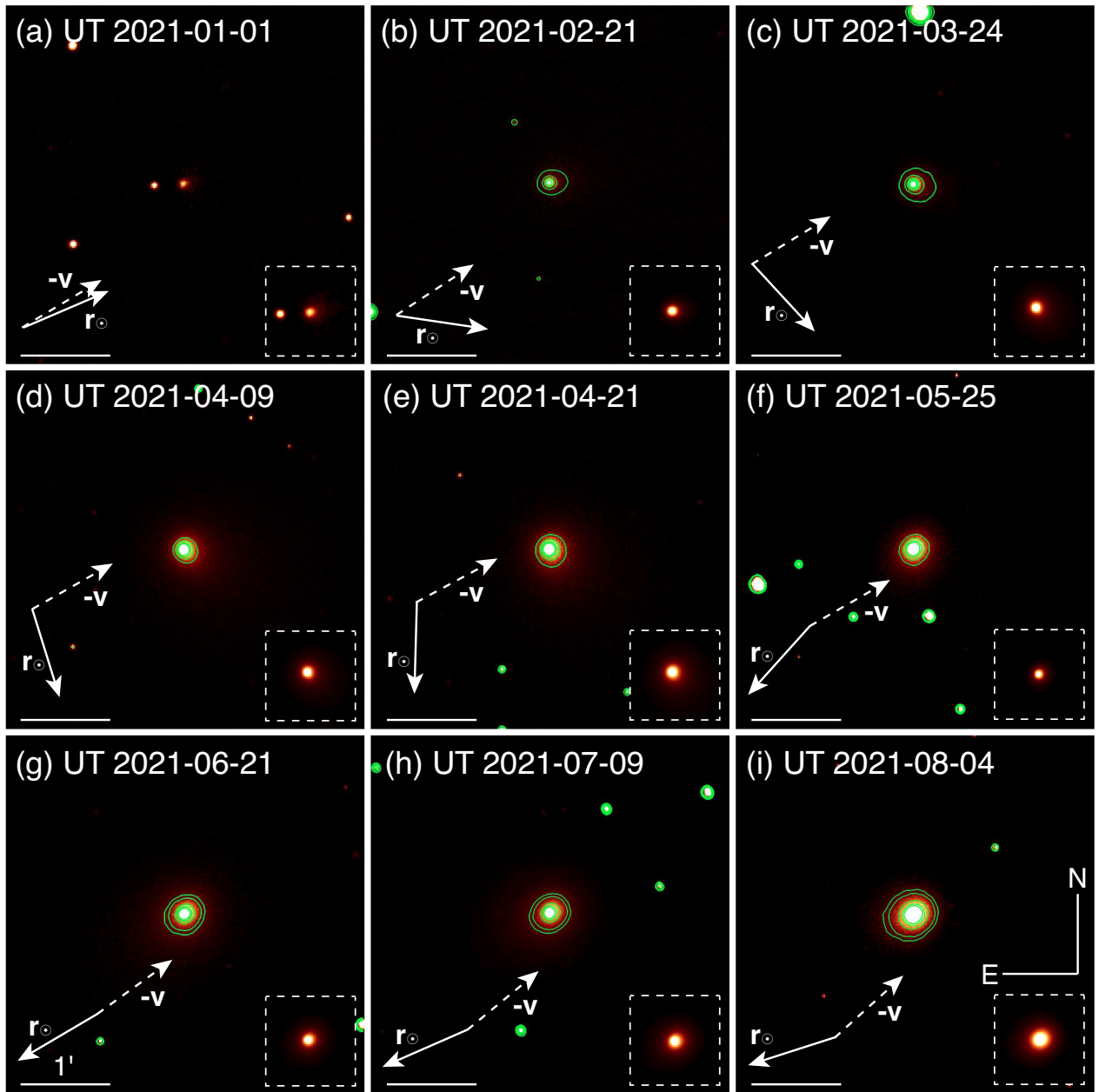


**Fig. A.1.** Coma morphology of T2 in its inbound (Panels a to h) and outbound (Panel i) orbit taken from the ZTF archive. All panels cover a FoV of  $4' \times 4'$  and provide a close-up image on the bottom right with FoV of  $1'$ . The negative velocity vector ( $-\mathbf{v}$ ), solar radius vector ( $\mathbf{r}_{\odot}$ ), and  $1'$  scale bar are given in each panel. A zoom-in image was processed by the boxcar smoothing with a width of 3 pixels to better visualize coma features. Five contour levels stratify the brightness within  $2\text{-}\sigma$  of the peak brightness on a logarithmic scale, except for the image on Panel a where we could not make aperture photometry due to its weak contrast to the background signal. The heliocentric distance for the comet in each panel is (a) 3.004 au (inbound), (b) 2.624 au (inbound), (c) 2.422 au (inbound), (d) 2.329 au (inbound), (e) 2.267 au (inbound), (f) 2.129 au (inbound), (g) 2.068 au (inbound), (h) 2.055 au (inbound, two days before perihelion), and (i) 2.075 au (outbound). North is up and east is to the left.

**Table B.1.** Properties of the comets used in Figure 6 and their references

Dyn. Type	Comet Name	$1/a_{\text{ori}}$ ( $10^{-6} \text{ au}^{-1}$ )	$1/a_{\text{osc}}$ ( $10^{-6} \text{ au}^{-1}$ )	$q_{\text{osc}}$ (au)	$i_{\text{osc}}$ ( $^{\circ}$ )	Obs. Type	References	
							Dyn. Type	Obs. Type
Oort-spike comets	C/1940 R2 (Cunningham)	-60.010	-1380.070	0.368	49.895	I	(1)	(4)
	C/1956 R1 (Arend-Roland)	19.740	-784.895	0.316	119.944	II	(2)	(5)
	C/1973 E1 (Kohoutek)	19.930	-54.835	0.142	14.304	II	(2)	(6), (7)
	C/1989 Q1 (OLR)	42.900	-86.684	0.642	90.146	I	(1)	(7), (8)
	C/1989 X1 (Austin)	40.840	-652.084	0.350	58.956	I	(1)	(7), (9)
	C/1993 A1 (Mueller)	61.840	-950.152	1.938	124.878	II	(1)	(7), (10)
	C/1999 S4 (LINEAR)	-54.510	-141.544	0.765	149.385	II	(2)	(11)
	C/2001 Q4 (NEAT)	60.560	-715.260	0.962	99.643	II	(1)	(9), (12)
	C/2002 T7 (LINEAR)	25.650	-791.285	0.615	160.583	II	(1)	(13)
	C/2003 K4 (LINEAR)	31.390	-293.766	1.024	134.253	I	(1)	(14), (15)
	C/2007 N3 (Lulin)	29.310	13.510	1.212	178.374	I	(1)	(16), (17)
	C/2007 W1 (Boattini)	-29.120	-0.0003	0.850	9.890	I	(1)	(15), (18)
	C/2011 L4 (PANSTARRS)	29.480	-108.664	0.302	84.208	II	(2)	(17)
	C/2012 S1 (ISON)	-36.060	-408.744	0.013	62.163	I	(1)	(19), (20)
	C/2013 US10 (Catalina)	52.960	-340.367	0.823	148.878	I	(2)	(21), (22)
C/2013 V1 (Boattini)	27.670	-859.225	1.661	65.310	II	(2)	(23)	
C/2017 K2 (PANSTARRS)*	35.490	-226.514	1.800	87.543	II	(1)	(24)	
Long-period comets	C/1957 P1 (Mrkos)	2000.790	1865.108	0.355	93.957	II	(2)	(25), (26)
	C/1974 C1 (Bradfield)	581.990	528.562	0.503	61.285	II	(2)	(27), (28)
	C/1975 N1 (KBM)	816.400	-215.618	0.426	80.781	I	(2)	(29), (30)
	C/1983 H1 (IAA)	10680.070	10200.506	0.991	73.251	I	(2)	(7)
	C/1987 P1 (Bradfield)	6379.200	6056.545	0.869	34.088	II	(2)	(30), (31)
	C/1988 A1 (Liller)	4880.400	4084.722	0.8841	73.322	II	(2)	(28), (32)
	C/1990 K1 (Levy)	113.630	-620.174	0.939	131.584	II	(1)	(30), (33)
	C/1991 T2 (Shoemaker-Levy)	936.350	166.289	0.836	113.497	II	(2)	(28)
	C/1992 F1 (Tanaka-Machholz)	3422.100	3189.030	1.262	79.292	II	(2)	(34)
	C/1995 O1 (Hale-Bopp)	3838.980	5492.937	0.917	89.217	II	(2)	(35), (36), (37)
	C/1996 B2 (Hyakutake)	1546.310	470.642	0.230	124.922	II	(2)	(38), (39)
	C/1996 Q1 (Tabur)	1876.000	1652.840	0.840	73.356	I	(3)	(40)
	C/2000 WM1 (LINEAR)	532.510	-437.171	0.555	72.550	II	(2)	(41), (42)
	C/2001 A2 (LINEAR)	1110.600	395.174	0.779	36.487	I	(2)	(43), (44)
	C/2004 Q2 (Machholz)	419.150	413.831	1.205	38.589	I	(2)	(45)
	C/2009 P1 (Garradd)	421.010	-643.289	1.551	106.177	II	(2)	(46)
	C/2012 L2 (LINEAR)	2540.640	1767.598	1.509	70.981	II	(2)	(47)
	C/2013 R1 (Lovejoy)	2722.000	1939.842	0.812	64.041	II	(3)	(48)
	C/2013 UQ4 (Catalina)	17209.130	16509.594	1.081	145.259	II	(2)	(49)
	C/2020 T2 (Palomar)	2778.000	3193.207	2.055	27.873	I	(2)	This Study
C/2014 S3 (PANSTARRS) <sup>†</sup>	11809.130	10879.747	2.050	169.321	I	(2)	(50)	
C/2013 P2 (PANSTARRS) <sup>†</sup>	1284.720	387.375	2.835	125.532	I	(2)	(51)	
A/2018 V3 <sup>†</sup>	8557.000	8234.440	1.340	164.977	I	(2)	(52)	
C/2002 CE10 (LINEAR) <sup>†</sup>	101736.630	101875.559	2.047	145.459	I	(2)	(53)	
C/2016 VZ18 (PANSTARRS) <sup>†</sup>	5090.920	5138.714	0.910	24.036	I	(2)	(54)	
C/2017 O1 (ASASSN) <sup>†</sup>	2477.000	2385.485	1.499	39.848	I	(2)	(55)	

**Notes.** Numbered references indicate (1) the Polish Catalogue of Near-Parabolic Comets ([http://ssdp.cbk.waw.pl/LPCs/near\\_parabolic\\_comets\\_catalogue.html](http://ssdp.cbk.waw.pl/LPCs/near_parabolic_comets_catalogue.html)); (2) Minor Planet Centre Database Search ([https://www.minorplanetcenter.net/db\\_search](https://www.minorplanetcenter.net/db_search)); (3) the Nakano Note (<https://www.oaa.gr.jp/~oaaacs/nk.htm>); (4) Öhman (1941); (5) Finson & Probst (1968b); (6) A'Hearn (1975); (7) Hanner et al. (1994); (8) Rosenbush et al. (1994); (9) Kwon et al. (2021); (10) Levasseur-Regourd et al. (1996); (11) Kiselev et al. (2002); (12) Wooden et al. (2004); (13) Rosenbush et al. (2006); (14) Woodward et al. (2004); (15) Velichko et al. (2012); (16) Woodward et al. (2011); (17) Roy Choudhury et al. (2015); (18) Gibb et al. (2012); (19) Wooden et al. (2014); (20) Snios et al. (2016); (21) Kwon et al. (2017); (22) Woodward et al. (2021); (23) Deb Roy et al. (2015a); (24) Zhang et al. (2022); (25) Kearns (1958); (26) Martel (1960); (27) Ney (1974); (28) Kiselev et al. (2015); (29) Ney (1982); (30) Chernova et al. (1993); (31) Hanner et al. (1990); (32) Turner & Smith (1999); (33) Lynch et al. (1992); (34) Geyer et al. (1996); (35) Kiselev & Velichko (1997); (36) Mason et al. (2001); (37) Harker et al. (2002); (38) Kiselev & Velichko (1998); (39) Mason et al. (1998); (40) Harker et al. (1999); (41) Joshi et al. (2003); (42) Kelley et al. (2004); (43) Rosenbush et al. (2002); (44) Furusho et al. (2003); (45) Velichko et al. (2005); (46) Hadamcik et al. (2014); (47) Deb Roy et al. (2015b); (48) Borisov et al. (2015); (49) Ivanova et al. (2017); (50) Meech et al. (2016); (51) Meech et al. (2014); (52) Piro et al. (2021); (53) Sekiguchi et al. (2018); (54) Bufanda et al. (2020); (55) Brinkman (2020). <sup>†</sup> Manxes or Manx candidates. \* Although the observations conducted within 3.1 au from the Sun have not been published, several studies observing the comet outside the water ice line (e.g. Yang et al. 2021; Fulle et al. 2022) and optical images from amateurs inside the line (e.g. <https://cometografia.es/2017k2-panstarrs-2022-07-15/#more-14767>) support its membership in Type II. We will present more detailed narrowband imaging and polarimetric aspects of its dust in our future work.

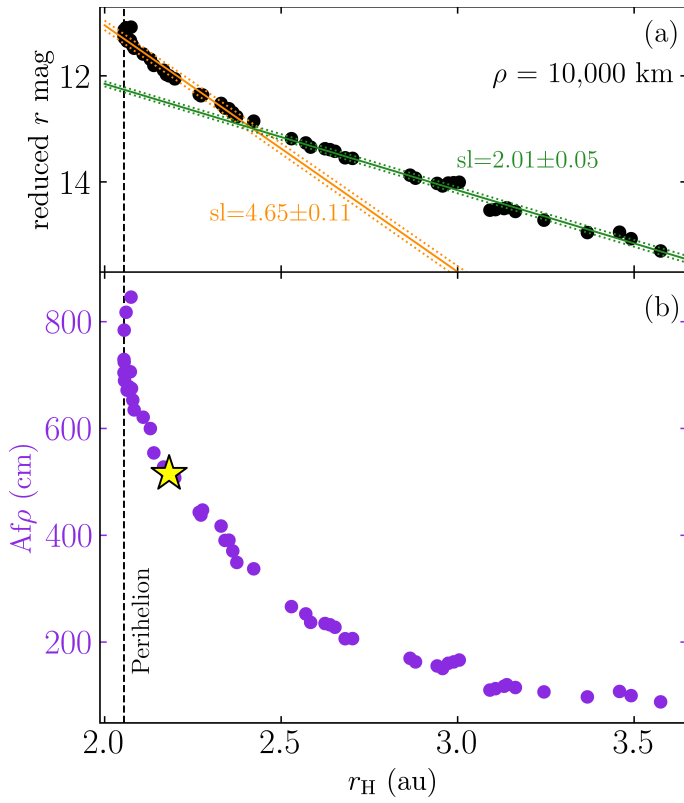


**Fig. A.2.** Secular evolution of the reduced  $r$ -band magnitude (Panel a) and  $Af\rho$  parameter (Panel b) as a function of heliocentric distance  $r_H$ . All points correspond to the photometric parameters measured from the aperture size of 10 000 km from the comet nucleus. The star symbol in Panel b denotes the time of our spectropolarimetric observation (UT 2021 June 26.2). The vertical dashed line indicates the perihelion distance at  $r_H = 2.055$  au. An increase in the brightness of T2 accelerates around 2.4 au from the Sun. A linear least-square fit to the heliocentric evolution of the reduced  $r$  magnitudes gives different slopes ('sl' in panel a) before and after the acceleration.